ELECTRONS AND COSMIC RAY PRODUCED PROTONS IN SATURN'S INNER MAGNETOSPHERE

T. G. Northrop
NASA/Goddard Space Flight Center
Greenbelt, MD 20771

and

Walker Fillius
Center for Astrophysics and Space Sciences
University of California San Diego
La Jolla, CA 92093

ABSTRACT

The University of California Cerenkov detector on Pioneer 11 previously observed Crand protons above 600 MeV in Saturn's inner magnetosphere, mixed with a poorly understood background of energetic electrons [Fillius and McIlwain, 1980]. Here we separate the electron from the proton counts and establish the first-order angular distributions for each species. To do this we use the theoretical relationships among the harmonic coefficients of the count rate as a function of spacecraft roll angle derived by Northrop [1985]. The majority of the counts were electrons with energy above several MeV; ie, with drift periods shorter than the satellite orbital resonance. The electrons have isotropic pitch angle distributions, and the protons pancake over most of the region between Mimas and the rings, although there is a small region of dumbbell proton distributions in the vicinity of Janus and Epimetheus.

INTRODUCTION

There was an internal inconsistency in the data taken at Saturn by the University of California, San Diego Cerenkov detector on Pioneer 11. East-west anisotropies observed between the outer edge of the A ring at 2.28 R_S and Mimas at 3.09 R_S apparently belonged to protons below the known response range of the detector. In the original analysis, Fillius and McIlwain deduced the gyroradius by using Liouville's theorem to interpret the radial displacement necessary to align the measured eastbound and westbound fluxes. The discrepancy was tentatively attributed to the presence of background electrons, but there was no method to quantify the contribution of these particles. Here we use the theory developed by Northrop in the accompanying paper to decompose the Cerenkov detector output into two components, belonging to high-rigidity protons and low-rigidity electrons. With this analytical tool we can give estimates of the proton and electron fluxes and, to a limited extent, their angular distributions. The results revise the high end of the energy spectrum of trapped protons created by the Crand mechanism, and reveal the existence of energetic electrons whose spatial distribution is unlike that of the lower energy electrons.

To show the instrumental dilemma we first present an essential description of the detector and relevant calibrations. From the proton response we conclude that the east-west anisotropy was produced by protons of energy ~600 MeV. Because the energy spectrum of the electron background is not well determined, we also include a description of the electron response in order to evaluate two different possibilities. Then we review the observations briefly, and show how we apply Northrop's method to separate the particle species.

PROTON RESPONSE OF THE CERENKOV DETECTOR

The UCSD Cerenkov detector on Pioneers 10 and 11 has a radiator of 60/40 methanol/water with index of refraction of 4/3. The liquid is held in a 14 X 75 mm bottle of ultra-pure fused silica the front end of which is occupied by an expansion bellows for thermal compensation between the liquid and the bottle. The radiator is viewed at one end by a photomultiplier tube and associated electronics which count pulses above three discrimination levels (labeled C1, C2, and C3). No coincidence detectors are used because the high fluxes of Jupiter's radiation belts would have paralyzed the necessary circuitry. Instead, directionality is achieved by internal reflection of light emitted toward the photomultiplier, and absorption of light traveling in the other direction on the bellows and blackened inner walls of the radiator housing. The discrimination levels are set so that the lowest channel (C1) can be triggered by a particle whose pathlength in the radiator is not much more than a diameter, but the highest channel (C3) requires a pathlength comparable to the length of the radiator. Thus the channels have different angular responses, from C1 with significant side sensitivity, to C3 with a pencil lobe in the forward direction only.

The angular response of the Cerenkov detector was demonstrated with an identical unit in the proton beam of the NASA Space Radiation Effects Laboratory (SREL) synchrocyclotron. The detector was rotated and its effective cross-sectional area was normalized to that of a monitor detector. Figure 1 shows the effective area vs angle from the detector look axis for channel C3.

When operating in a space radiation environment, the detector is irradiated simultaneously from all angles, and here the most useful calibration is the integral of the effective area over solid angle, called the geometric factor,

$$G(E) = \int A_{eff}(E)\, d\Omega$$

Figure 2 shows the geometric factor as a function of energy for several discrimination levels. Because the principal effect of varying the discrimination level is to vary the pathlength needed to yield enough light, the principal difference between channels is in the width of their angular

responses, and so, in the magnitude of their geometric factors. The energy threshold is a second-order effect because all protons near the threshold easily have enough range to penetrate the entire detector and thus to produce the same pathlength. The channel to channel differences in energy threshold are primarily due to the fact that the lower channels are able to respond to Cerenkov light produced in the bottle walls and faceplate. For the index of fused silica, 3/2, the critical proton energy is 320 MeV. This accounts for the incipient response evident in channels C1 and C2 in Figure 2, but it is not a major factor because, with only a small amount of fused silica, it requires exceptionally favorable particle trajectories.

The peak energy of the SREL synchrocyclotron was not high enough to complete the response curve of the detector. To calibrate the asymptotic high-energy response, we used cosmic ray muon counting rates observed in our laboratory, corrected for the effect of the muon angular distribution over the angular response of the detector. These asymptotic geometric factors are plotted on the right-hand axis of Figure 2.

The channels labeled C1, C2, and C3 in figure 2 were matched to the prelaunch discrimination levels of the Pioneer 10 and 11 Cerenkov detectors. Both of these detectors underwent subsequent gain changes because of the high level radiation during the Jovian encounter. The effect on the Pioneer Cerenkov detector was to increase the photomultiplier tube gain, which is equivalent to lowering the discrimination levels. The channel in Figure 2 marked C3′ is interpolated from C2 and C3 to the level of Pioneer 11 channel C3 during the Saturn encounter.

The small lump at ~100 MeV is caused by scintillation of protons that stop in the optical materials. As mentioned by Fillius and McIlwain [1980], this represents an omnidirectional geometric factor of $< .002$ cm^2 for protons between 65 and 140 MeV. By comparison, the UCSD solid state detector on Pioneer 11 has a geometric factor of .012 cm^2 over a larger energy window between 80 and several hundred MeV. Then by comparing the counting rates of these two sensors, we can conclude that no more than about 12%, of the C3 response is caused by proton scintillation.

ELECTRON RESPONSE OF THE CERENKOV DETECTOR

The Cerenkov detector is also sensitive to electrons. (Its primary mission was to measure the intensities of high energy electrons in the Jovian environment.) Figures 3 and 4 show the measured electron response. For electrons, unlike protons, penetration range is an important factor in understanding the detector response. The first important threshold is the energy (~0.7 MeV) required for an electron to penetrate the detector housing. Since electrons are relativistic at this energy, the next criterion is the length of their track in the radiator, which determines their Cerenkov light output. As with protons, the particle trajectory must point toward the back end of the radiator in order to direct the Cerenkov beam to the cathode. The electrons' propensity to undergo high-angle scattering collisions has two effects. One is that the range tends to be understated by tables which list "end-point values," or the range of a scatterfree particle, and the other is that the angular responses tend to be smeared.

Figure 3 demonstrates the net result for channel C3. Full response occurs at high energy where the particles' range exceeds the length of the radiator and the relativistic mass gain reduces their tendency to scatter. The biteout along the axis has two causes. One is that the asymptotic Cerenkov emission angle equals the critical reflection angle, so that light starts to be lost. The other is that there is more passive shielding at the front end of the housing than on the sides. As the electron energy decreases, the dominant response occurs on the side, where the radiator has a larger cross-sectional area, but smaller depth. Ultimately, as the electron energy decreases, the pulse height falls below the discrimination level. Then the electrons can only trigger the detector if several arrive simultaneously so that their pulses add in height. In this mode the response is peaked to the side where the cross-sectional area is largest. Channels C1 and C2 operated in this mode during the most intense segment of the Saturn flyby.

Figure 4 shows the geometric factor for single-particle events, plotted as a function of energy. This represents the detector's response to a delta function energy spectrum. It is convenient to represent this profile as a step function, so that we can quote the flux above some threshold. We

previously used Van Allen's "bow-tie method" to obtain such a representation applicable to the Jovian radiation environment [Fillius and McIlwain, 1974]. However, at Saturn, the electrons causing the pileup on channels C1 and C2 have an extremely soft spectrum, outside the range of anything encountered previously. As the bowtie method showed, the same threshold value is not applicable for all spectra. Therefore, we have listed in Table I threshold energies applicable to a range of power law energy spectra, of the form,

$$dN/dE = - K E^{-n}$$

This table should help in interpreting the detector's response to very soft electron spectra.

Table I

Threshold energies for channel C3
usable for different power law energy spectra
with a geometric factor of 0.5 cm^2-sr

n	E_{th}
1	14
2.5	14
4	12
6.3	10
10	8.5

OBSERVATIONS

The channel C3 counting rate reached a maximum in the vicinity of 2.7 R_S ($1R_S$ = 60,000 km) and fell off to zero and near-zero values at the outer edge of the A ring (2.28 R_S) and the orbit of Mimas (3.09 R_S). The east-west anisotropies that we are investigating are associated with the gradients on either side of the peak. Using a least-squares fitting procedure, Fillius and McIlwain [1980] represented the angular distribution of the counting rate by a truncated Fourier expansion of the form $C = C_0 + C_1\sin(\chi) + C_2\cos(2\chi) +$

$C_3\sin(3\chi) + \ldots$, χ being the angle between the look direction of the detector and the magnetic field, which happened to lie in the scan plane. Terms were chosen for symmetry and economy: omitted terms would violate mirror symmetry, and coefficients above 3χ were so heavily convolved by the width of the sampling interval that they could not be evaluated with our limited amount of data. In this representation the coefficient C_0 is the spin-averaged count rate; the omnidirectional count rate is $C_0 - C_2/3 - C_4/15$. The coefficient C_2 reflects whether the peak of the distribution is perpendicular to the magnetic field ($C_2 < 0$) or parallel to it ($C_2 > 0$). The former case is called a pancake distribution and the latter, a dumbbell. The east-west anisotropy appears in the odd harmonics C_1 and C_3.

The coefficients derived from the data are shown in Figures 5 and 6 for the inbound and outbound radial cuts of Pioneer 11. The smooth curves were merely drawn by eye through the points. Note that outbound C_0 and C_2 have quite similar shapes, and inbound they are similar, too, although the peaks are not quite coincident. In Figure 6 there was a data gap between 2.38 R_s and 2.49 R_s. This has been filled in by interpolation so as to be able to carry out integrals over the entire range. Results inside 2.49 R_s outbound are therefore not to be trusted and will not be given in later figures.

SEPARATION OF PROTON FROM ELECTRON COUNTS

The observed coefficients are assumed to be sums of proton and electron components. Thus $C_0 = C_{0p} + C_{0e}$, and similarly for the higher harmonic coefficients. We assume that there is no pile-up in this channel and no counts lost to dead time. In the preceding paper Northrop [1985] derived relationships among the harmonic coefficients of the proton and electron count rate as a function of roll angle. Because the electrons have very small gyroradius, their odd harmonics vanish, and the odd harmonics observed are attributed entirely to protons. The even proton coefficients are given by equations (14) and (15) of that paper:

$$C_{2p}(r) = C_{4p}(r) + 2r^6 \left[\frac{r_1^3}{\rho_p(r_1)\cos\theta} \int_{r_1}^{r} dy \frac{C_{3p}(y)}{y^9} + 9 \int_{r_1}^{r} dy \frac{C_{4p}(y)}{y^7} \right] \quad (1)$$

$$C_{0p}(r) = \frac{C_{4p}(r)}{2} + \frac{r_1^3}{\rho_p(r_1)\cos\theta} \left[\int_{r_1}^{r} dy \frac{C_{1p}(y) - C_{3p}(y)}{y^3} + 2r^6 \int_{r_1}^{r} dy \frac{C_{3p}(y)}{y^9} \right]$$

$$+ 6 \int_{r_1}^{r} dy \frac{C_{4p}(y)}{y} \left(\frac{3r^6}{y^6} - 1 \right) \quad (2)$$

where r_1 is some point at which the count rate vanishes (say the outer edge of the A ring), and $\rho_p(r_1)$ is the proton gyroradius at r_1. Based on the detector calibrations (See Figures 1 and 2), we used a proton energy of 600 MeV to calculate the gyroradius. The integrals were performed by Simpson's rule upon the smooth curves. This is a bit subjective, but, unlike differentiation, integration tends to even out random errors in the input. Once C_{0p} and C_{2p} are known, C_{0e} and C_{2e} are given by $C_{0e} = C_0 - C_{0p}$ and $C_{2e} = C_2 - C_{2p}$.

Coefficient C_4 is absent from Figures 5 and 6 because there were not enough data to determine it directly as a function of r. We have assumed that C_4 has the same shape as the other even coefficients and determined the ratio $b = C_4/C_0$ from the integral conditions (16) and (17) of the preceding paper. The conditions use the fact that the fluxes vanish at both boundaries of the region of interest. This method gives two values for b, one from each equation, and unless they agree, there is a dilemma. We find that inbound b = 0.0915 and 0.0881 from (16) and (17) respectively. This minor discrepancy is handled by using 0.0915 in (1) and 0.0881 in (2) -- that is, by using b in the

equation from which it was determined. One may prove that the value of (1) or (2) is independent of whether one integrates from r_2 inward, or from r_1 outward to the r of interest, provided that the b used in the equation was determined from it. Outbound the two values of b determined from (1) and (2)disagree: (1) gives b = 0.00467 and (2) gives b = -0.0130. In this case we have again used the b in the equation from which it came. The disagreement may be a consequence of the data gap.

Figures 7 and 8 give the omnidirectional count rates for protons and electrons, and Figures 9 and 10 are the pitch angle distributions to lowest order in gyroradius. (The f_0 from equation 3 of the preceding paper.) We immediately see that the proton count rate was only 20% of the electron rate. The proton angular distribution is found to be pancake (except in the vicinity of Janus and Epimetheus where they are dumbbell) and the electrons are isotropic. Both angular distributions agree with what one expects from cosmic rays as the source, striking ring material in the case of the protons, or the moons Mimas, Janus, Epimetheus, and rings for electrons [Blake et al., 1983]. That cosmic rays produce protons by the Crand process in the inner region of Saturn's magnetosphere was first suggested by Fillius et al. [1980] and also by Cooper and Simpson [1980], Van Allen et al. [1980], and McDonald et al. [1980]. Other papers have subsequently studied the pitch angle distribution. If that distribution is modeled by $\sin^n(\delta)$, a value of n=6 at 3.5 R_s has been reported by Vogt et al, [1982]. Krimigis and Armstrong [1982] find n=5. Schardt and McDonald [1983] find that for 48-160 MeV protons n increases from ~1 at 2.7 R_s to nearly 5 at 2.85 R_s.

DISCUSSION: INBOUND DATA

The peak of the proton omnidirectional flux occurs at larger radial distance than the electron peak. (There is no theoretical reason for the peaks to coincide.) That there should be a proton peak is to be expected: Crand is a distributed source of protons, and the A ring, Janus-Epimetheus, and Mimas are sinks for the protons, which diffuse both ways from the interior of the region under study. Cooper [1983] has solved the problem of the Crand source plus diffusion to absorbing edges and fit the University of Chicago

data from Pioneer 11. From Figure 7 the peak for 600 MeV protons is at 2.72 R_s, and there is a minimum at 2.52 R_s caused by proton absorption by Janus and Epimetheus, leaving a secondary peak at 2.4 R_s that is about 1/3 the height of the main peak. The position of the main peak and the factor of 1/3 both coincide with the profiles determined by Van Allen et al [1980] and Fillius and McIlwain [1980] for energies > 80 MeV. There is no discernible absorption by the G-ring at these >600 MeV energies, in contrast to lower energies where all experiments see an effect (See, for example, Van Allen [1983]).

The proton angular distributions (Figure 9) are pancake outside the Janus-Epimetheus absorption, and are dumbbell in the minimum, as would be expected from preferential wipeout of equatorial particles. The upswing at low count rates of these angular distributions is probably not real, nor are negative values. There is much scatter in these deduced distributions, which is not surprising considering the long train of analysis. The proton distribution goes approximately as $\sin^5(\delta)$ at the peak (2.72 R_s), but we cannot determine any trend at larger radii, although theory predicts more isotropy [Cooper, 1983].

In contrast to protons, there is no significant volume source of electrons of the proper energy within the region. Two different sources of electrons are possible. High energy electrons are produced by cosmic rays at the rings and at Mimas, [Blake et al., 1983] and diffuse toward the center of the region from these sources at the two edges. The energy of these electrons is tens of MeV, and so they are well up on the plateau of the detector response (See Figure 4). The strength of this source is unknown, and it is not clear that there should be a peak at 2.62 R_s, given the location of the sources.

Also, electrons from other sources, outside Mimas, may be diffusing inward. The spectrum of these electrons is soft, because the preferred energy for electrons to escape absorption by Mimas is just 1 MeV, and by 7 MeV the relative drift time has fallen from infinity to <5 hours. As compiled by Chenette and Stone [1983], the electron spectrum at Mimas falls by 4 orders of magnitude between 5 MeV and 11 MeV. Magnetic-moment-conserving diffusion of relativistic electrons from Mimas to the electron peak at 2.62 R_s increases

the energy of electrons with 90° pitch angle by a factor of 1.3. With the steeply falling energy spectrum, this energization would increase the number of electrons above the energy threshold by a factor of 21. The count rates at Mimas were small, at most a few per second, so it seems that a peak of 315 per second is too large to be accounted for completely in this way.

In sum, we do not know what fraction of the electrons are produced by cosmic rays at Mimas and the rings, and what fraction by other processes elsewhere.

OUTBOUND DATA

The electron peak is comparable in height with the inbound electron peak but is at a larger radius than inbound. As inbound, the electron angular distributions are quite isotropic. The radial profile of the electrons is different from that observed at lower energies, in that it is peaked, and vanishes at the orbits of Mimas and at the F ring. At lower energies (~1 MeV) the electrons do not exhibit clear channels at the orbits of these moons, which is consistent with their resonant energy to avoid sweeping.

The peak in proton flux in Figure 8 is at the same radius (2.72 R_s) as inbound and is at just about the same height. As at lower energies (e.g., above 80 MeV [Van Allen et. al, 1980; Fillius and McIlwain, 1980]) there appears to be azimuthal symmetry about Saturn. Although we have no data inside 2.49 R_s, there is no evidence in Figure 8 of an incipient upturn of the curve inward of 2.5 R_s. Van Allen does see wings of a secondary peak outbound that he estimates would have been lower than inbound by a factor of 2 to 3. He suggests that such an inbound-outbound asymmetry may be connected with the longitude of moons such as Janus and Epimetheus relative to that of Pioneer inbound and outbound.

The proton angular distributions are pancake except near Janus and Epimetheus where they are dumbbell -- just as was the case inbound. The pancake distributions are less well organized than inbound. We do not know whether this is real or merely represents the noise in the analysis, which is

not completely satisfying because of the determination of C4 and the data gap. Nevertheless, the results of the analysis agree remarkably well with the inbound pass, and with observations at lower energies (>80 MeV).

CONCLUSIONS

1. We have employed the method developed by Northrop in the accompanying paper [1985], for deducing the omnidirectional intensity and first-order angular distributions of high-rigidity particles in the presence of a background of low-rigidity particles. The method is applied by performing appropriate integrals over the observed angular distributions, and can be thought of as an integration of the radial gradient deduced from the east-west anisotropy of the high-rigidity particles.

2. We have evaluated the number of 600 MeV protons necessary to produce the east-west anisotropy observed by the UCSD Cerenkov detector on Pioneer 11 between 2.3 and 3.1 R_s. This is a significant downward revision of the estimate made by Fillius and McIlwain [1980], but nevertheless still consistent with other data at lower energies. Crand is the most likely source for these particles, as concluded by Fillius and McIlwain [1980].

3. There exists a high energy component of the electron spectrum which has a spatial profile with low values at Mimas and Janus-Epimetheus and a maximum in between. This profile indicates that sweeping takes place at these moons, which is to be expected for electrons of several MeV or more. The source and spectrum of these electrons remains uncertain.

4. We have determined the pitch angle distributions of these particles to first order in gyroradius. The electrons are almost isotropic, but the protons exhibit a combination of pancakes and dumbbells, with the latter near Janus and Epimetheus.

ACKNOWLEDGEMENTS

We thank J. B. Blake and S. H. Margolis for several discussions, and J. A. Van Allen for supplying us with details of his Pioneer 11 observations in the inner magnetosphere. This work was supported in part by NASA Grants NAG W-336 and NAG W-652.

REFERENCES

Blake, J. B., H. H. Hilton, and S. H. Margolis, "On the Injection of Cosmic Ray Secondaries Into the Inner Saturnian Magnetosphere: 1. Protons From the Crand Process," J. Geophys. Res., 88, 803, 1983.

Chenette, D. L., and E. C. Stone, "The Mimas Ghost Revisited: An Analysis of the Electron Flux and Electron Microsignatures Observed in the Vicinity of Mimas at Saturn," J. Geophys. Res., 88, 8755, 1983.

Cooper, J. F., and J. A. Simpson, "Sources of High-Energy Protons in Saturn's Magnetosphere," J. Geophys. Res., 85, 5793, 1980.

Cooper, J. F., "Nuclear Cascades in Saturn's Rings: Cosmic Ray Albedo Neutron Decay and Origins of Trapped Protons in the Inner Magnetosphere," J. Geophys. Res., 88, 3945, 1983.

Fillius, W., W.-H. Ip, and C. E. McIlwain, "Trapped Radiation Belts of Saturn: First Look," Science, 207, 425, 1980.

Fillius, W., and C. E. McIlwain, "Very Energetic Protons in Saturn's Radiation Belt," J. Geophys. Res., 85, 5803, 1980.

Krimigis, S. M., and T. P. Armstrong, "Two Component Proton Spectra in the Inner Saturnian Magnetosphere," Geophys. Res. Lett., 9, 1143, 1982.

McDonald, F. B., A. W. Schardt, and J. H. Trainor, "If You've Seen One Magnetosphere, You Haven't Seen Them All: Energetic Particle Observations in the Saturn Magnetosphere," J. Geophys. Res., 85, 5813, 1980.

Northrop, T. G., "Relationships Among the Harmonic Coefficients of Scan Plane Anisotropies," accompanying paper submitted to J. Geophys. Res., 1985.

Van Allen, J. A., B. A. Randall, and M. F. Thomsen, "Sources and Sinks of Energetic Electrons and Protons in Saturn's Magnetosphere," J. Geophys. Res., 85, 5679, 1980.

Vogt, R. E., D. L. Chenette, A. C. Cummings, T. L. Garrard, E. C. Stone, A. W. Schardt, J. H. Trainor, N. Lal, and F. B. McDonald, "Energetic Charged Particles in Saturn's Magnetosphere: Voyager 2 Results," Science, 215, 577, 1982.

FIGURE CAPTIONS

Figure 1

Effective Area of Cerenkov detector channel C3 as a function of angle to the detector axis for protons of energy 66, 98, 137, 446, 497, 521, and 560 MeV. The proton energy is given at the right hand edge of each curve. Because of experimental difficulties there is significant scatter and statistical error, and this is illustrated for 560 MeV (circles) and 98 MeV (crosses). These data were taken at the NASA Space Radiation Effects Laboratory (SREL).

Figure 2

Response vs energy for several pulse height channels of the UCSD Cerenkov detector. (For identification of the channels, see the text.) The proton response was obtained at SREL up to its peak energy of 560 MeV, and ground level cosmic ray muons were used to calibrate the asymptotic response of the detector to particles with = 1.

Figure 3

Effective area vs angle for electrons of the indicated energies.. These data were obtained on the electron linac operated by Intelcom Radtek Corporation in San Diego.

Figure 4

Response vs energy for channels C1, C2, and C3 of the UCSD Cerenkov detector. To represent these profiles as ideal step functions, one must allow the value of the threshold energy to depend upon the energy spectrum of the incident radiation. (See Table I and text.)

Figure 5

Harmonic coefficients of the count rate as a function of the spacecraft roll angle, plotted vs. radial distance to Saturn during the inbound pass.

(a) Even harmonics, inbound.

(b) Odd harmonics, inbound.

Figure 6

Harmonic coefficients of the count rate as a function of the spacecraft roll angle, plotted vs. radial distance to Saturn during the outbound pass.

(a) Even harmonics, outbound.

(b) Odd harmonics, inbound.

Figure 7

Derived omnidirectional count rates for protons and electrons on the inbound pass.

Figure 8

Derived omnidirectional count rates for protons and electrons on the outbound pass.

Figure 9

Derived angular distributions for protons and electrons on the inbound pass.

Figure 10

Derived angular distributions for protons and electrons on the outbound pass.

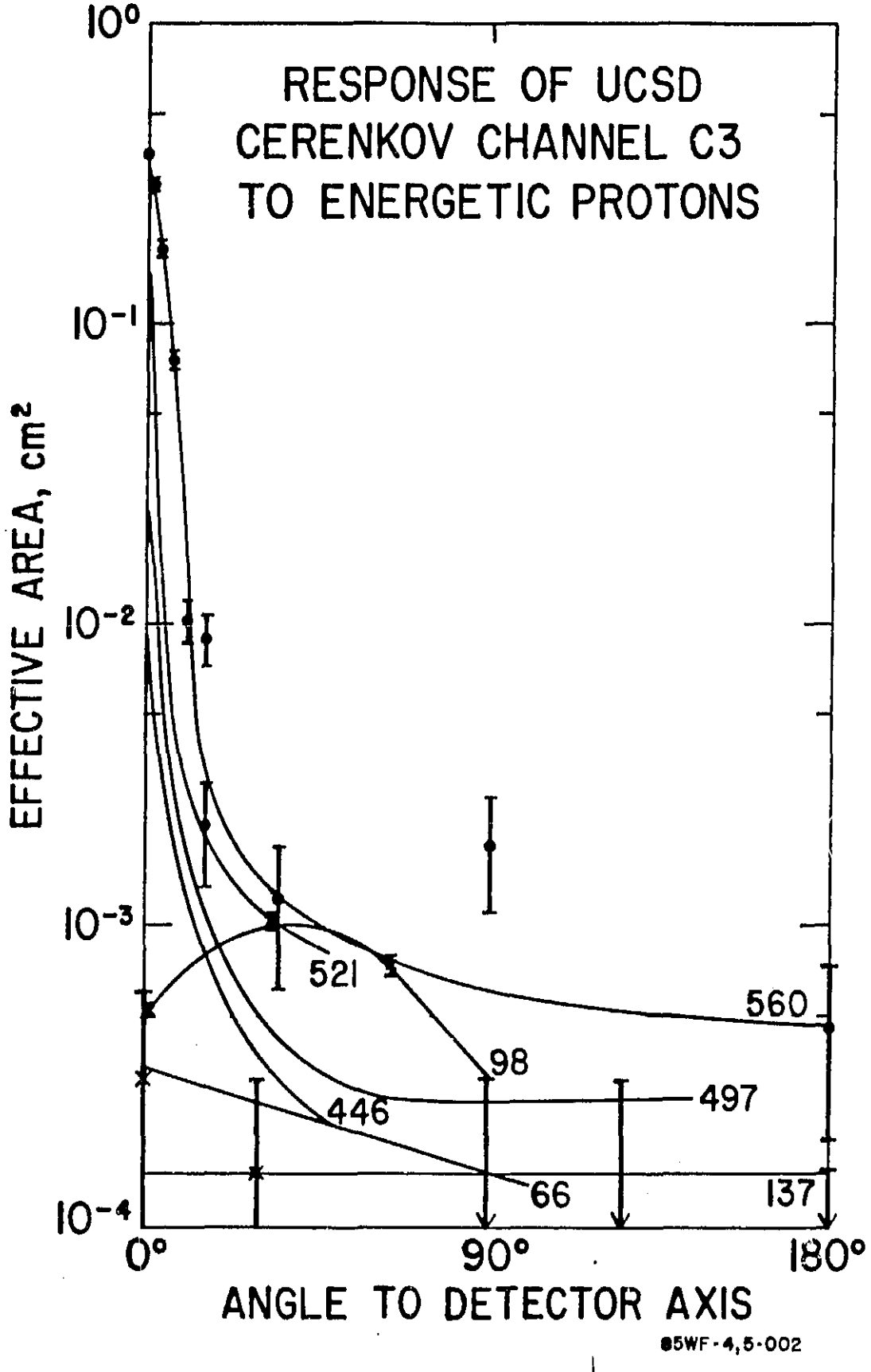
RESPONSE OF UCSD
CERENKOV CHANNEL C3
TO ENERGETIC PROTONS
EFFECTIVE AREA, cm²
10⁰
10⁻¹
10⁻²
10⁻³
10⁻⁴
521
560
98
497
446
66
137
0°
90°
180°
ANGLE TO DETECTOR AXIS
85WF-4,5-002

Fig. 1

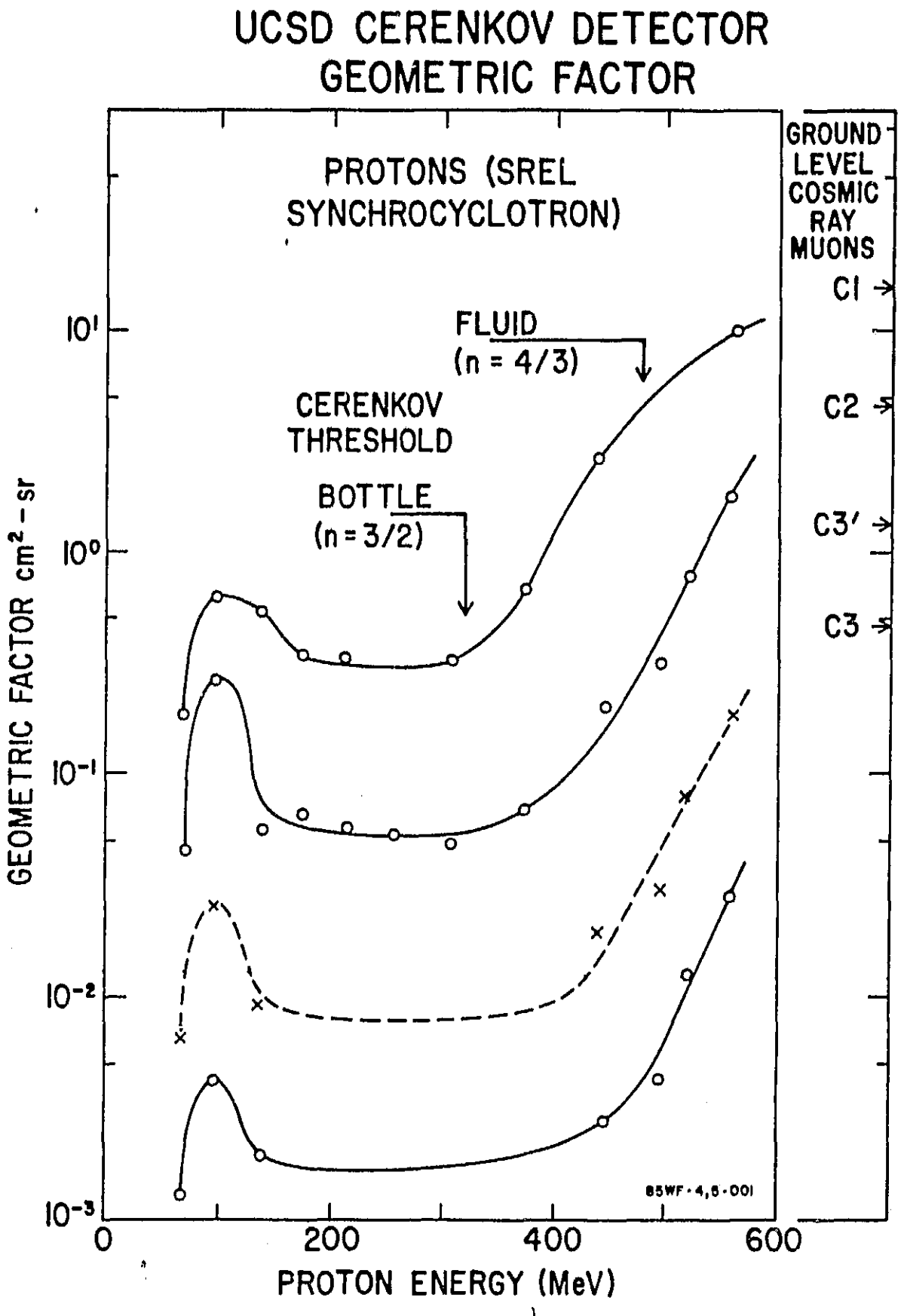
UCSD CERENKOV DETECTOR
GEOMETRIC FACTOR
PROTONS (SREL
SYNCHROCYCLOTRON)
GROUND
LEVEL
COSMIC
RAY
MUONS
C1
C2
C3'
C3
FLUID
(n = 4/3)
CERENKOV
THRESHOLD
BOTTLE
(n = 3/2)
GEOMETRIC FACTOR cm² - sr
10¹
10⁰
10⁻¹
10⁻²
10⁻³
0
200
400
600
PROTON ENERGY (MeV)
85WF-4,5-001

Fig. 2

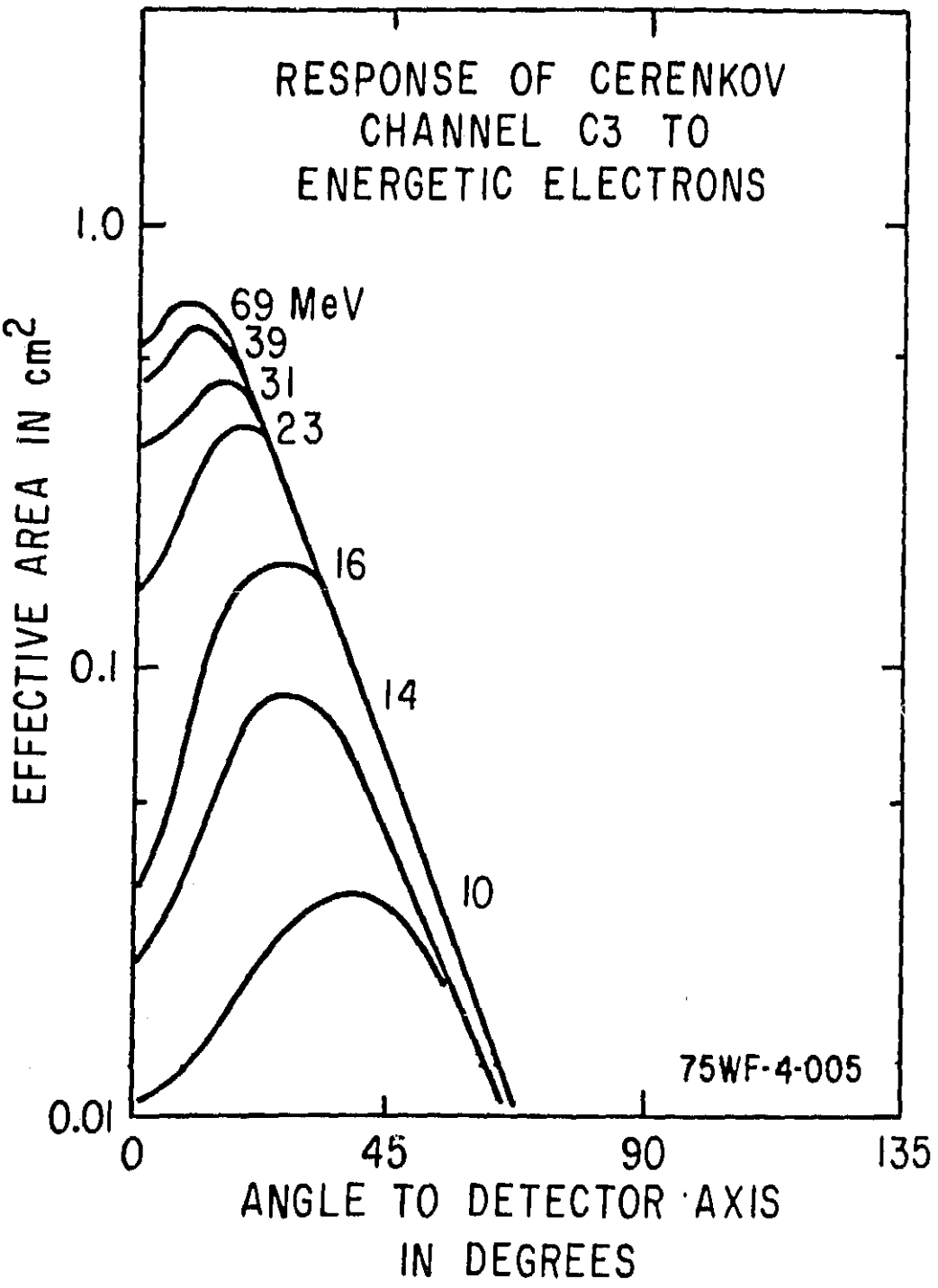
RESPONSE OF CERENKOV
CHANNEL C3 TO
ENERGETIC ELECTRONS
1.0
0.1
0.01
EFFECTIVE AREA IN cm²
69 MeV
39
31
23
16
14
10
75WF-4-005
0
45
90
135
ANGLE TO DETECTOR AXIS
IN DEGREES

Fig. 3

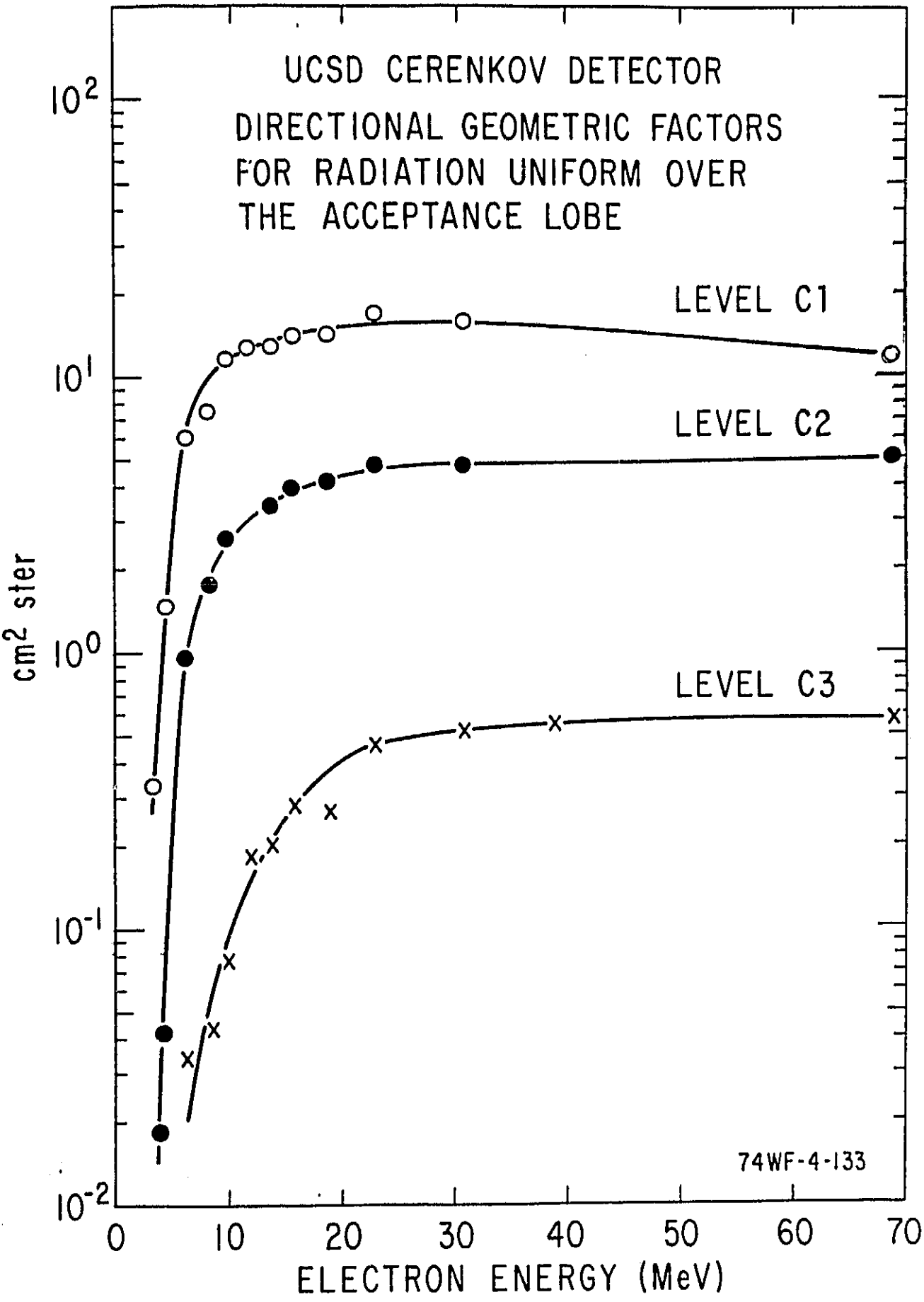
UCSD CERENKOV DETECTOR
DIRECTIONAL GEOMETRIC FACTORS
FOR RADIATION UNIFORM OVER
THE ACCEPTANCE LOBE
LEVEL C1
LEVEL C2
LEVEL C3
74WF-4-133
cm² ster
ELECTRON ENERGY (MeV)
10²
10¹
10⁰
10⁻¹
10⁻²
0
10
20
30
40
50
60
70

Fig. 4

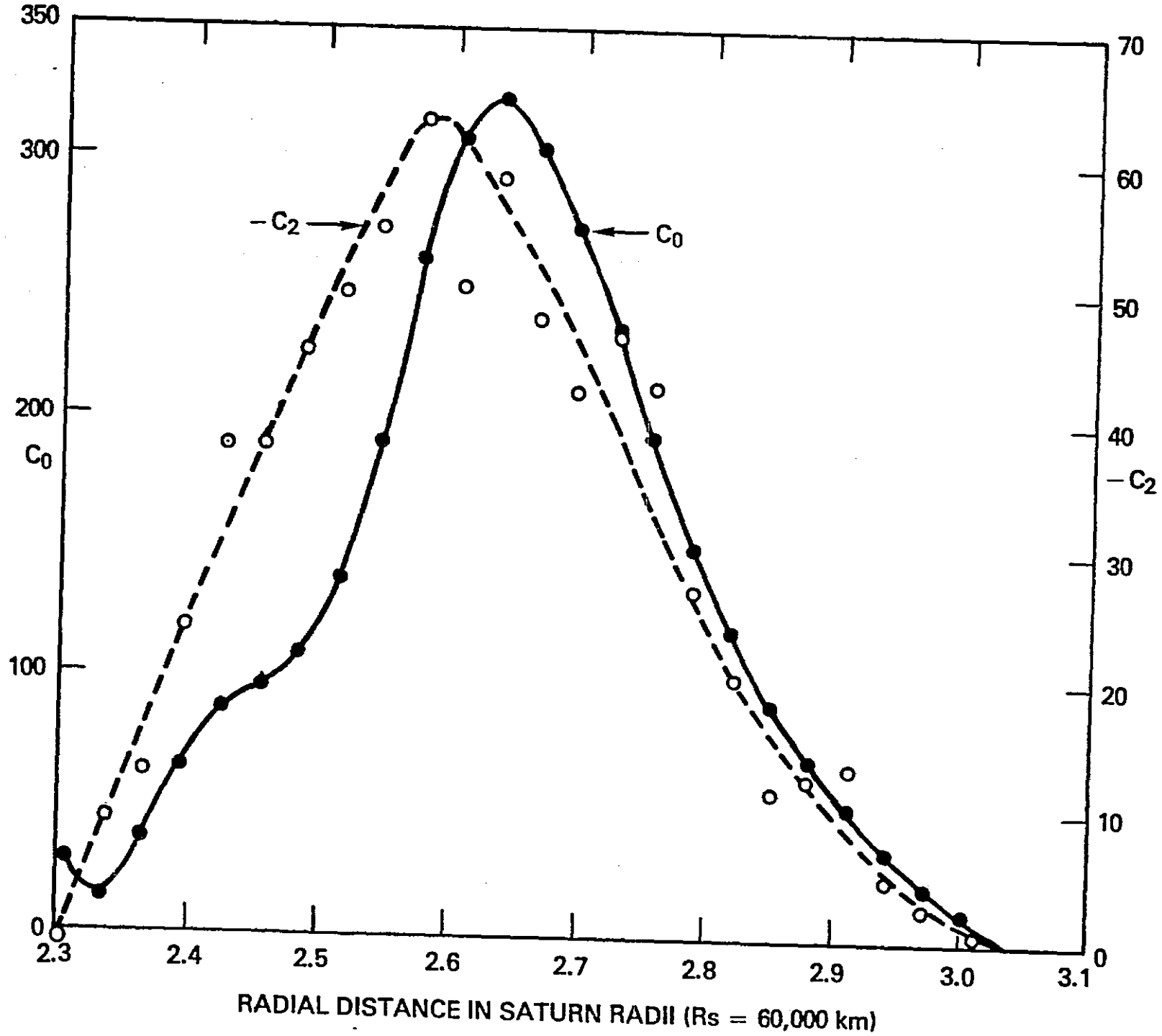
350
300
200
100
0
C_0
70
60
50
40
30
20
10
0
$-C_2$
$-C_2$
C_0
2.3
2.4
2.5
2.6
2.7
2.8
2.9
3.0
3.1
RADIAL DISTANCE IN SATURN RADII (Rs = 60,000 km)

Fig. 5a

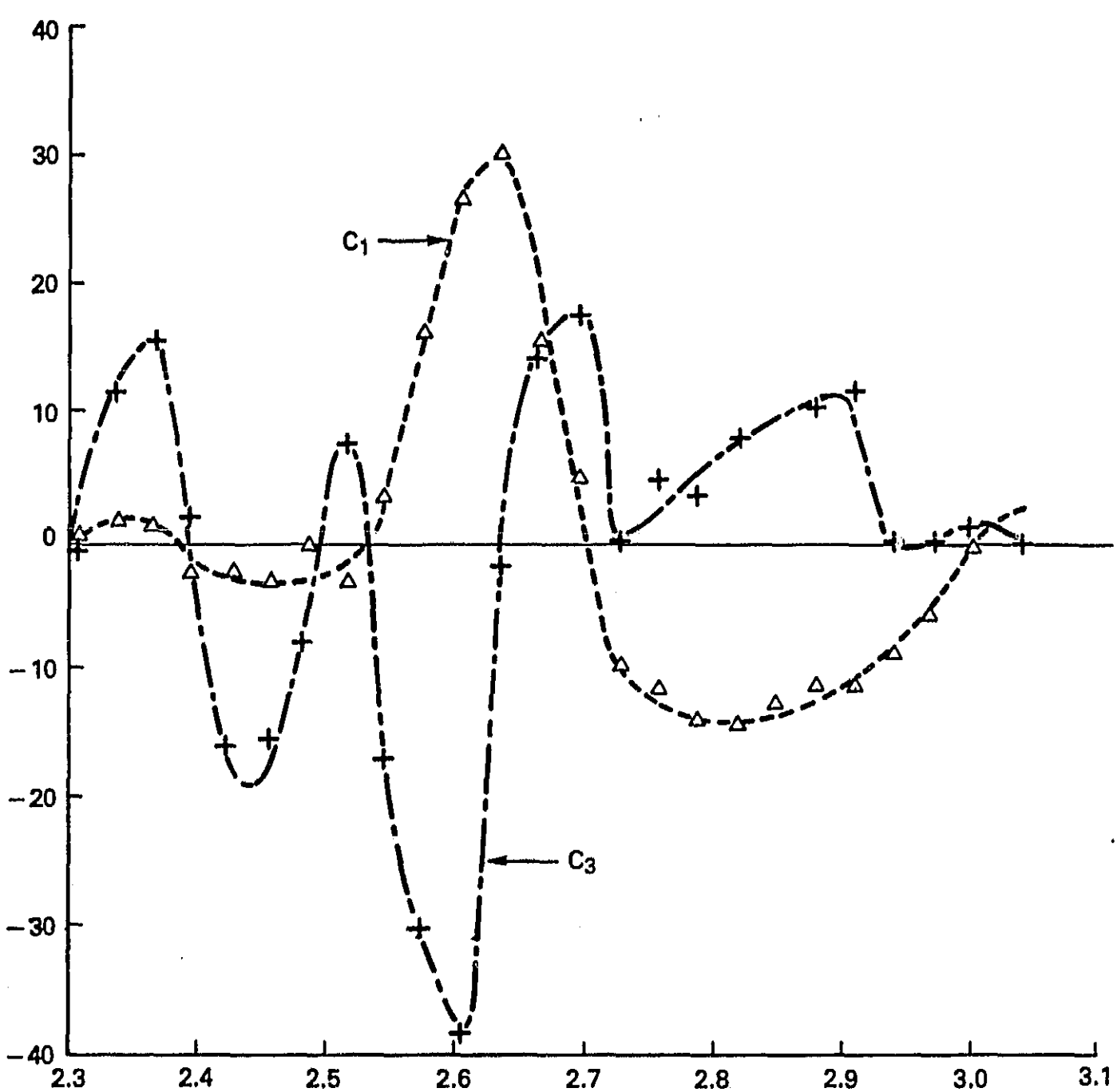
40
30
20
10
0
−10
−20
−30
−40
2.3
2.4
2.5
2.6
2.7
2.8
2.9
3.0
3.1
C1
C3
RADIAL DISTANCE IN SATURN RADII (Rs = 60,000 km)

Fig. 5b

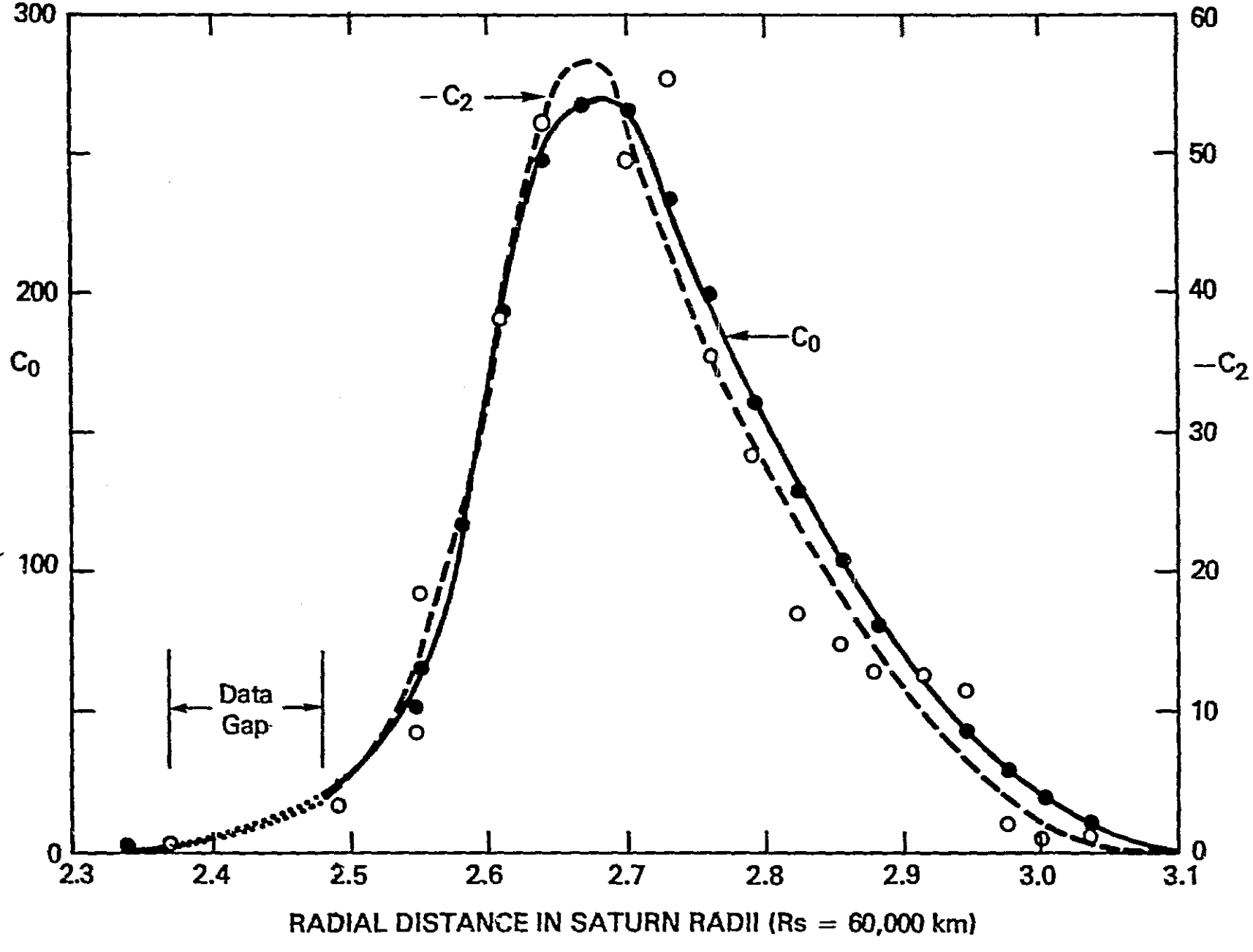
300
200
100
0
C_0
60
50
40
30
20
10
0
$-C_2$
$-C_2$
C_0
Data
Gap
2.3
2.4
2.5
2.6
2.7
2.8
2.9
3.0
3.1
RADIAL DISTANCE IN SATURN RADII (Rs = 60,000 km)

Fig. 6a

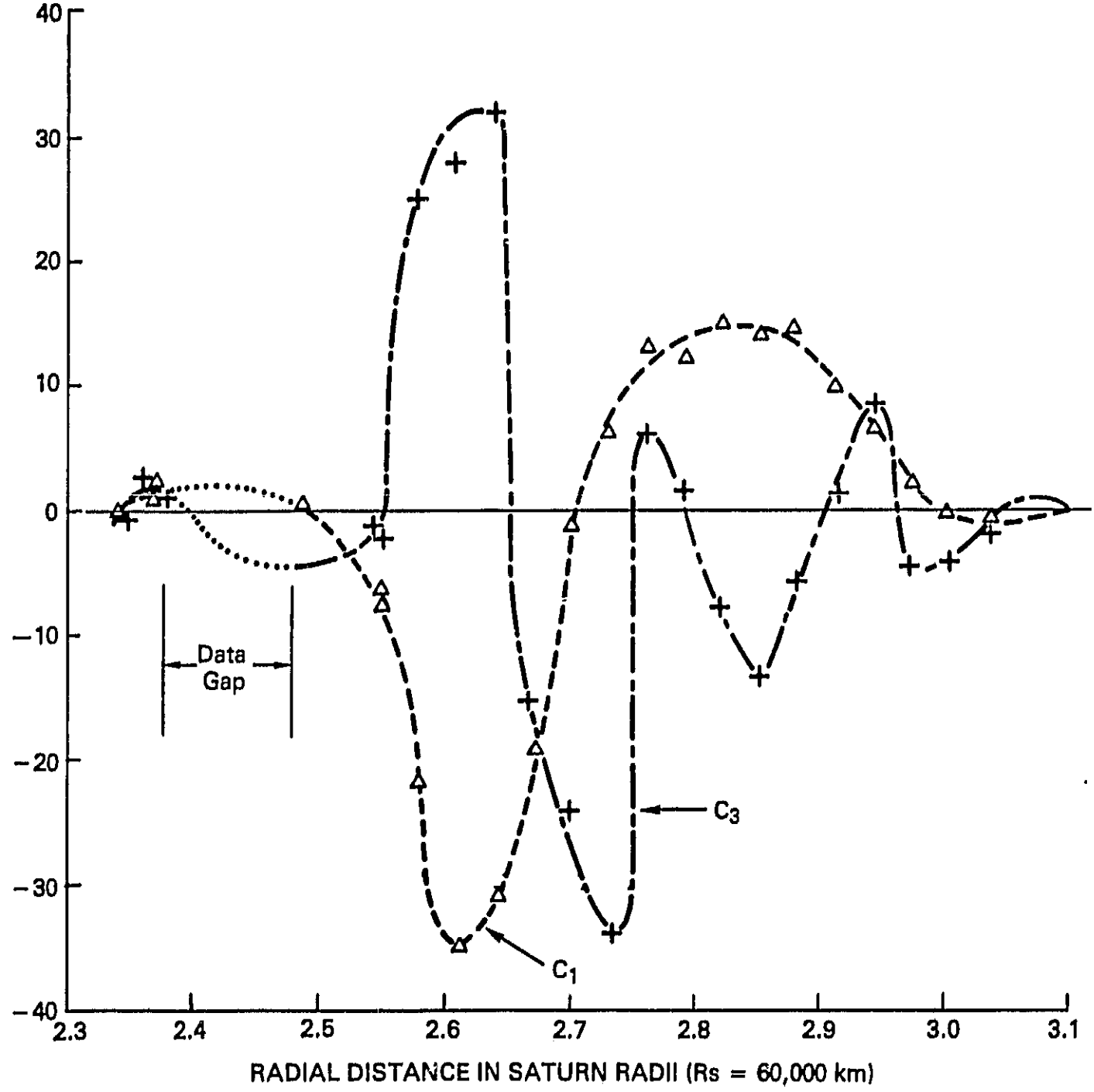
40
30
20
10
0
−10
−20
−30
−40
2.3
2.4
2.5
2.6
2.7
2.8
2.9
3.0
3.1
Data
Gap
C3
C1
RADIAL DISTANCE IN SATURN RADII (Rs = 60,000 km)

Fig. 6b

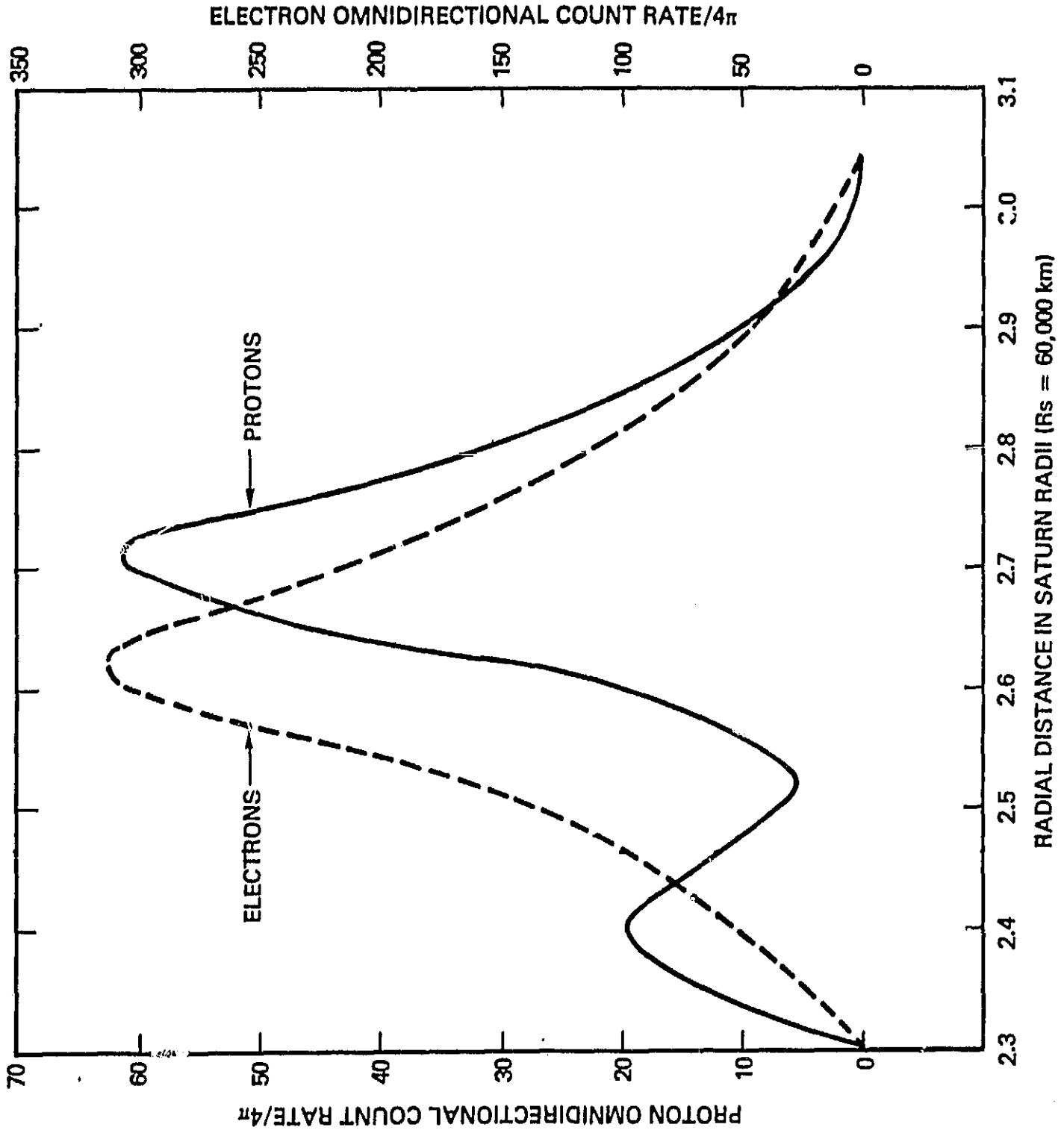
ELECTRON OMNIDIRECTIONAL COUNT RATE/4π
350
300
250
200
150
100
50
0
PROTONS
ELECTRONS
70
60
50
40
30
20
10
0
PROTON OMNIDIRECTIONAL COUNT RATE/4π
2.3
2.4
2.5
2.6
2.7
2.8
2.9
3.0
3.1
RADIAL DISTANCE IN SATURN RADII (Rs = 60,000 km)

Fig. 7

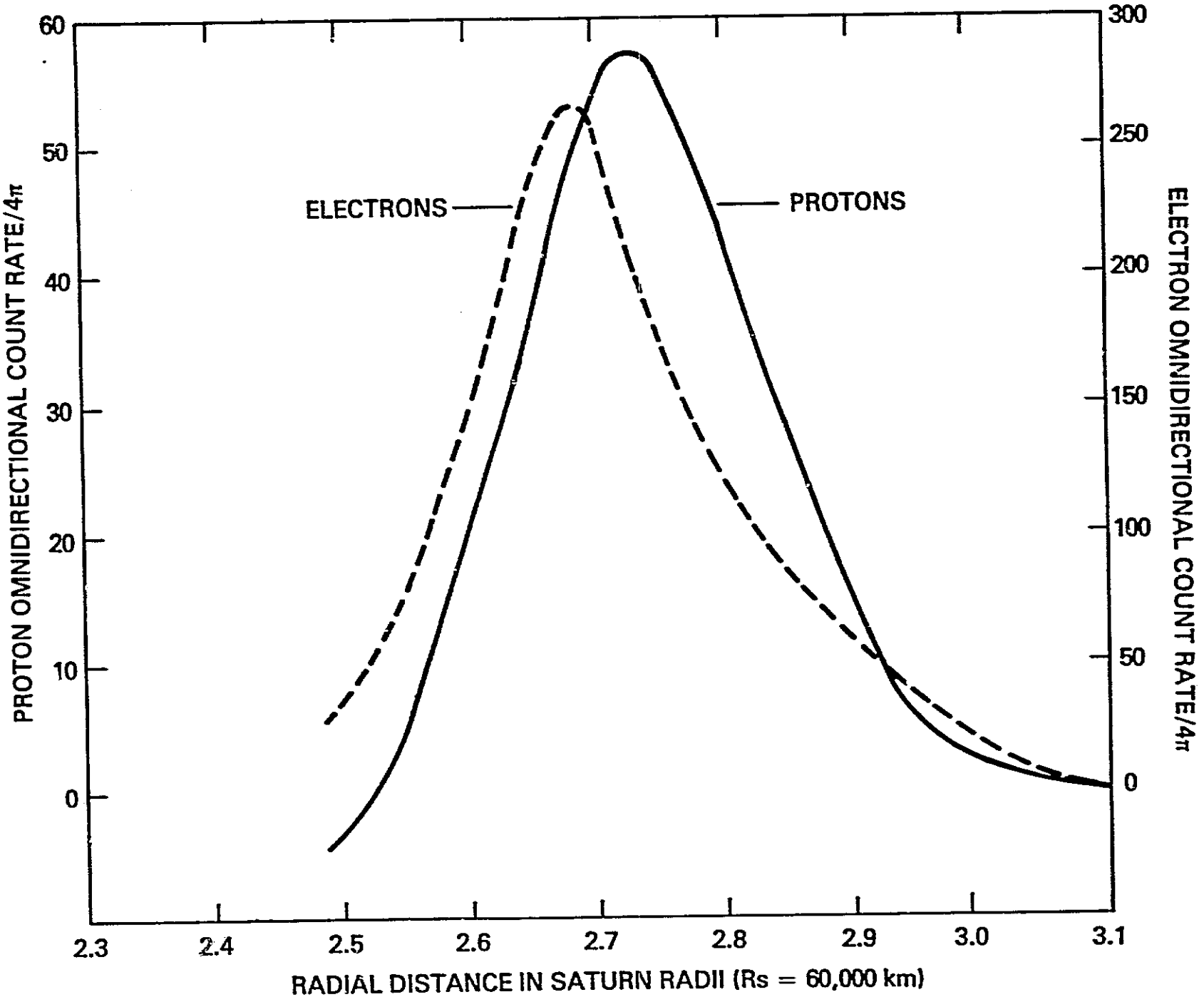
ELECTRONS
PROTONS
PROTON OMNIDIRECTIONAL COUNT RATE/4π
ELECTRON OMNIDIRECTIONAL COUNT RATE/4π
RADIAL DISTANCE IN SATURN RADII (Rs = 60,000 km)
60
50
40
30
20
10
0
300
250
200
150
100
50
0
2.3
2.4
2.5
2.6
2.7
2.8
2.9
3.0
3.1

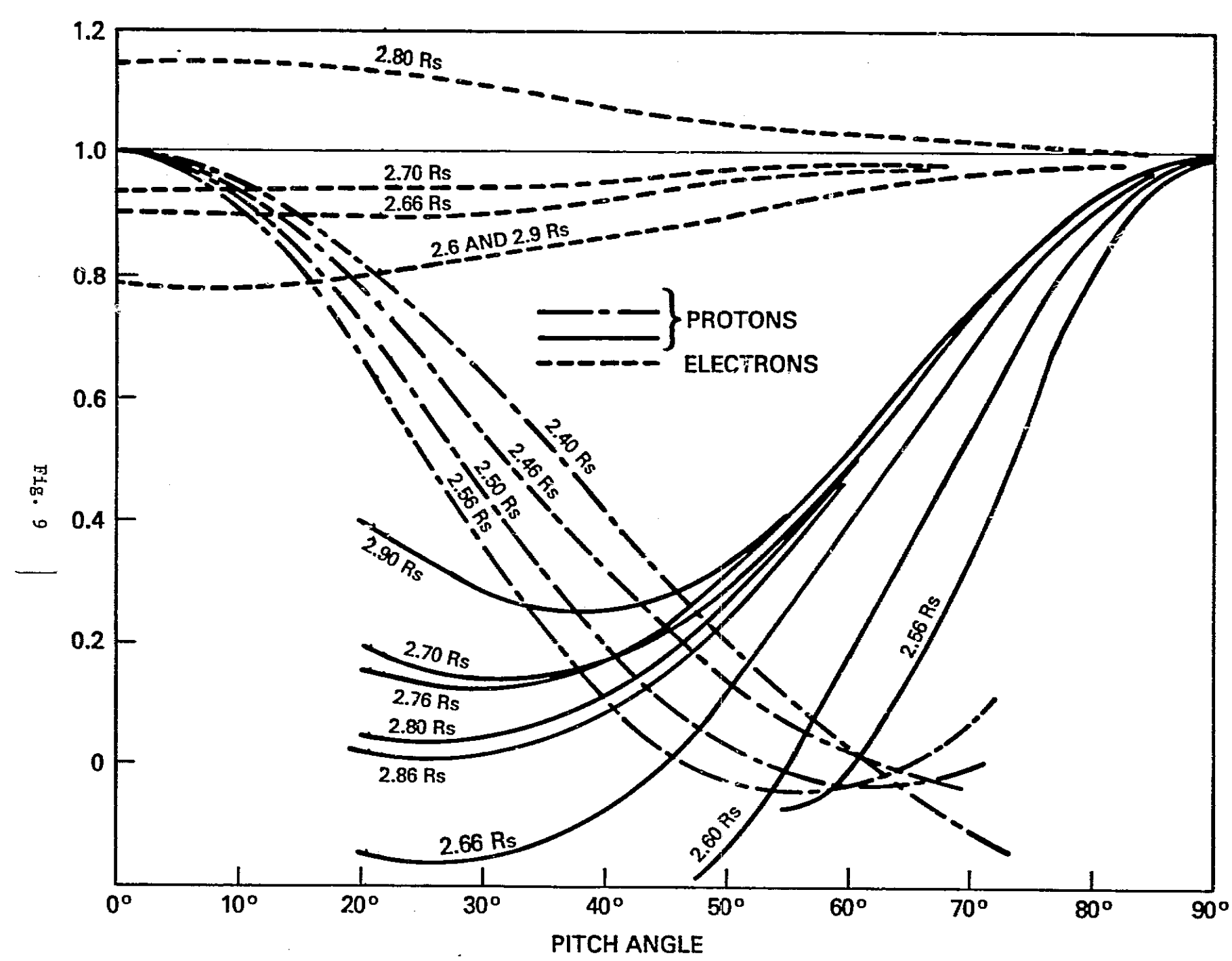
1.2
1.0
0.8
0.6
0.4
0.2
0
2.80 Rs
2.70 Rs
2.66 Rs
2.6 AND 2.9 Rs
PROTONS
ELECTRONS
2.40 Rs
2.46 Rs
2.50 Rs
2.56 Rs
2.90 Rs
2.70 Rs
2.76 Rs
2.80 Rs
2.86 Rs
2.66 Rs
2.56 Rs
2.60 Rs
0°
10°
20°
30°
40°
50°
60°
70°
80°
90°
PITCH ANGLE

FIG. 9

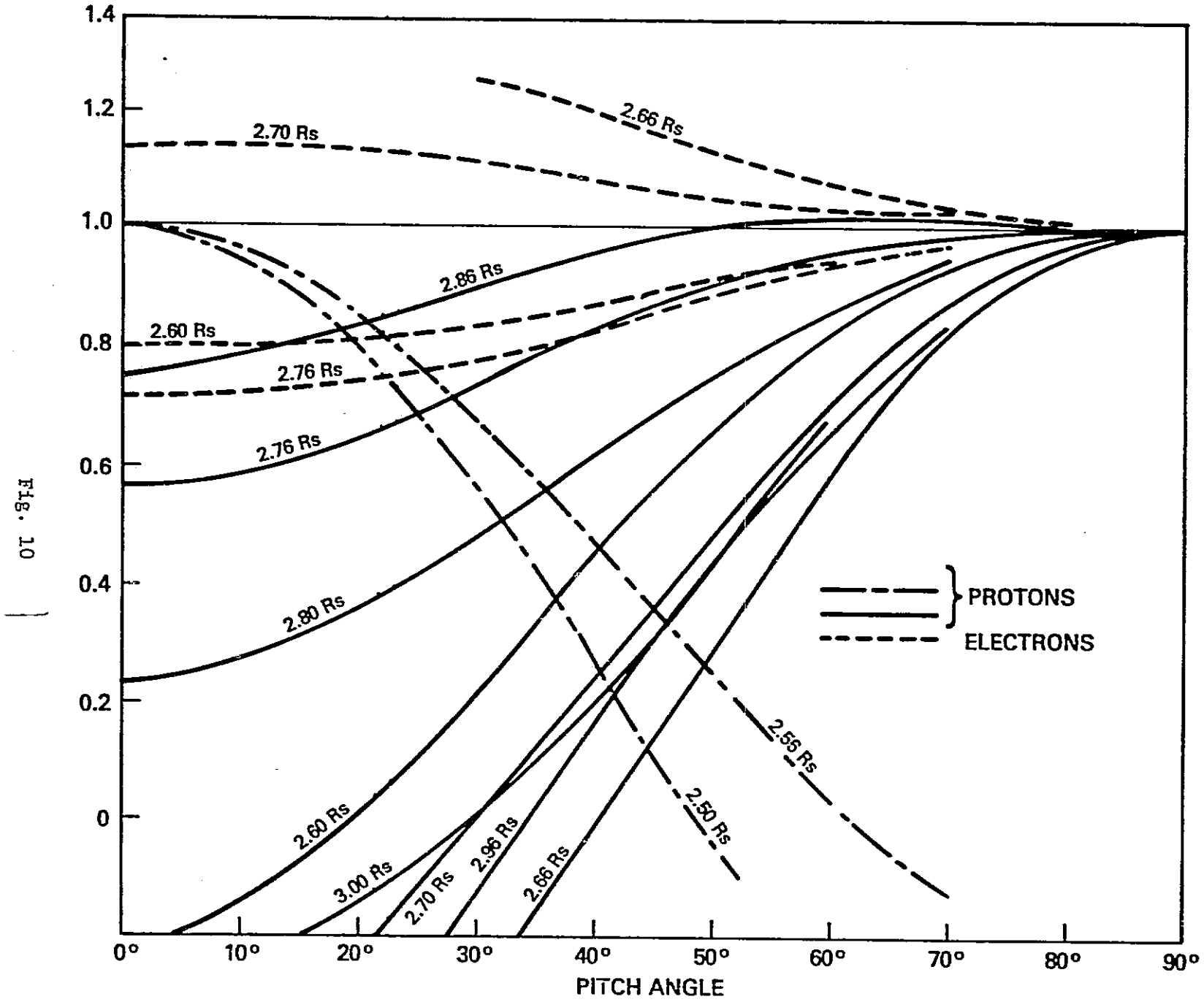
1.4
1.2
1.0
0.8
0.6
0.4
0.2
0
2.70 Rs
2.66 Rs
2.86 Rs
2.60 Rs
2.76 Rs
2.76 Rs
2.80 Rs
2.60 Rs
3.00 Rs
2.70 Rs
2.96 Rs
2.66 Rs
2.50 Rs
2.56 Rs
PROTONS
ELECTRONS
0°
10°
20°
30°
40°
50°
60°
70°
80°
90°
PITCH ANGLE

FIG. 10